Shedding Light on Metal-Based Nanoparticles in Zebrafish by Computed Tomography with Micrometer Resolution

*Emre Cörek, Griffin Rodgers, Stefan Siegrist, Tomaz Einfalt, Pascal Detampel, Christian M. Schlepütz, Sandro Sieber, Pascal Fluder, Georg Schulz, Harald Unterweger, Christoph Alexiou, Bert Müller, Maxim Puchkov, and Jörg Huwyler**

Metal-based nanoparticles are clinically used for diagnostic and therapeutic applications. After parenteral administration, they will distribute throughout different organs. Quantification of their distribution within tissues in the 3D space, however, remains a challenge owing to the small particle diameter. In this study, synchrotron radiation-based hard X-ray tomography (SRµCT) in absorption and phase contrast modes is evaluated for the localization of superparamagnetic iron oxide nanoparticles (SPIONs) in soft tissues based on their electron density and X-ray attenuation. Biodistribution of SPIONs is studied using zebrafish embryos as a vertebrate screening model. This label-free approach gives rise to an isotropic, 3D, direct space visualization of the entire 2.5 mm-long animal with a spatial resolution of around 2 µm. High resolution image stacks are available on a dedicated internet page (http://zebrafish.pharma-te.ch). X-ray tomography is combined with physico-chemical characterization and cellular uptake studies to confirm the safety and effectiveness of protective SPION coatings. It is demonstrated that SRµCT provides unprecedented insights into the zebrafish embryo anatomy and tissue distribution of label-free metal oxide nanoparticles.

1. Introduction

Engineered metal-based nanoparticles are increasingly used for medical applications, notably in the field of biomedical imaging.[1,2] In most cases, they consist of a metal or metal oxide core and a coating of organic materials such as polysaccharides, polypeptides, proteins, fatty acids or polyethyleneglycol (PEG) for chemical and colloidal stabilization.[3] Prominent examples are superparamagnetic iron oxide nanoparticles (SPIONs) which are clinically used as magnetic resonance imaging contrast agents.[4] In addition, application of an (alternating) external magnetic field for therapeutic purposes offers interesting perspectives in oncology, in that such nanoparticles can be used for a hyperthermia therapy or to target drug loaded particles to tumors. The latter is referred to as magnetic drug targeting.[5] In order to study the in vivo biodistribution of such particles, they have to be labeled by conjugation of fluorescent or radioactive agents. However, these chemical modifications can significantly change the interaction patterns with biological matter since they have a direct impact on particle size and polydispersity, electrokinetic potential (ζ-potential), and possibly the protein corona.[6–9] It is therefore recommended to carry out, whenever possible, physicochemical characterization, formulation development, pharmacokinetic studies, and hazard and safety evaluations with non-tagged nanoparticles.[10] In recent years, magnetic particle imaging (MPI), magnetic resonance imaging (MRI) or computed tomography[11] have been discussed as label-free alternative to trace engineered metal nanoparticles within a biological system. The latter technology takes advantage of their strong X-ray absorption.[12,13] In medical research, laboratory-based micro-computed tomography (µCT) has been used to monitor the biodistribution of metal-based nanoparticles in vitro or in small experimental animals.[13–16] A challenge

---

Dr. E. Cörek, Dr. S. Siegrist, Dr. T. Einfalt, Dr. P. Detampel, Dr. S. Sieber, P. Fluder, Dr. M. Puchkov, Prof. J. Huwyler
Department of Pharmaceutical Technology
University of Basel
Klingelbergstrasse. 50, Basel 4056, Switzerland
E-mail: joerg.huwyler@unibas.ch

The ORCID identification number(s) for the author(s) of this article can be found under https://doi.org/10.1002/smll.202000746.

DOI: 10.1002/smll.202000746

G. Rodgers, Dr. G. Schulz, Prof. B. Müller
Biomaterials Science Center
Department of Biomedical Engineering
University of Basel
E-mail: Gewerbestrasse 14, Allschwil 4123, Switzerland

Dr. C. M. Schlepütz
Swiss Light Source
Paul Scherrer Institute
Forschungsstrasse 111, Villigen 5232, Switzerland

Dr. H. Unterweger, Prof. C. Alexiou
Department of Otorhinolaryngology
Head and Neck Surgery, Section for Experimental Oncology and Nanomedicine (SEON), Else Kröner-Fresenius Stiftung Professorship
Erlangen University of Erlangen
Waldstraße 1, Erlangen 91054, Germany

is thereby the combination of a large field-of-view (to image an entire animal) and a relatively low resolution of the used detector arrays in the order of a few thousand pixels in width. In addition, large administered doses are needed to overcome density resolution limits, despite the fact that high doses may cause artefacts. Therefore, detecting medically relevant metal-based nanoparticle concentrations within intact whole-body samples remains a major challenge.

It was therefore the aim of the present study to address these issues by using synchrotron radiation-based micro computed tomography (SRμCT) in phase and absorption contrast modalities to study the biodistribution of non-labeled SPIONs within a soft tissue sample. To this end, the zebrafish embryo was used as a test system. The zebrafish embryo has been widely discussed as predictive vertebrate screening model for nanotoxicology in recent years.[17,18] It has several benefits over alternative in vivo models such as optical transparency, 78% genetic homology with humans, cost-efficiency, small size (less than 0.5 mm in diameter, less than 5 mm in length), and an immune system similar to humans.[19] Our team has extensively used zebrafish embryos to study the pharmacokinetics and tissue distribution of particulate drug carriers.[20] SRμCT offers higher density and spatial resolution than conventional laboratory μCT thanks to higher brilliance. It should be noted that the high intensity synchrotron X-ray beam allows for incorporation of a monochromator providing a tunable beam source. Consequently, no beam hardening correction is necessary to obtain quantitative absorption data and phase contrast accessibility.[21] In this study, we demonstrate that low doses of sterically stabilized SPIONs can indeed be localized within the whole zebrafish embryo by SRμCT. The offered micrometer resolution allowed for detailed 3D image reconstruction of the small (≈2.5 mm) vertebrate embryos. Furthermore, it was possible to detect within these soft tissue specimens deposits of iron oxide nanoparticles.

2. Results

2.1. Synthesis of SPIONs

Coating of iron oxide nanoparticles is important to ensure colloidal stability in solution and to prevent particle erosion.[3] The iron oxide core of the SPIONs was synthesized by coprecipitation in a one-pot synthesis resulting in particles with a narrow particle size distribution.[22] Subsequently, four types of surface modifications were introduced. Hydrophilic macromolecules, that is, dextran and human serum albumin, were deposited on the SPION surface giving rise to HSA-SPIONs[23] or Dex-SPIONs.[24] Alternatively, particles were embedded within a phospholipid bilayer (Lipid-SPIONs) or a lipid shell containing pegylated phospholipids (sterically stabilized Lipid-PEG-SPIONs) using a microfluidics approach.[25]

Reference particles were fluorescent labeled in the case of Lipid-SPIONs and Lipid-PEG-SPIONs. HSA-SPIONs and Dex-SPIONs were produced using good manufacturing practice (GMP) compliant protocols. It was therefore neither desired nor possible to deviate from the manufacturing process and to introduce a fluorescent label.

Table 1. Physico-chemical characterization of superparamagnetic iron oxide nanoparticles (SPIONs). Human serum albumin coated iron oxide nanoparticles (HSA-SPIONs), Dextran-coated iron oxide nanoparticles (Dex-SPIONs), phospholipid embedded iron oxide nanoparticles (Lipid-SPIONs), and modified phospholipid embedded iron oxide nanoparticles with PEG of molecular weight 5000 (Lipid-PEG-SPIONs) were characterized by dynamic and electrophoretic light scattering. Hydrodynamic diameter, polydispersity index (PDI), and the electrokinetic potential (ζ-potential) of the particles were determined using phosphate-buffered saline as a diluent. Where indicated, particles were fluorescent labeled. Values are means ± SD, *n* = 3.

Particle	Hydrodynamic diameter [nm]	PDI[a)]	ζ-potential [mV]	Fluorescent label
HSA-SPIONs	61 ± 0.4	0.14	–35.7 ± 1.0	No
Dex-SPIONs	70 ± 0.3	0.17	–18.4 ± 3.1	No
Lipid-SPIONs	100.8 ± 0.6	0.26	–42.3 ± 2.8	No
Lipid-PEG-SPIONs	89.2 ± 0.5	0.23	–22.5 ± 1.2	No
Lipid-SPIONs	91 ± 0.5	0.24	–41.6 ± 2.0	Yes
Lipid-PEG-SPIONs	81.5 ± 0.5	0.22	–20.6 ± 1.4	Yes

[a)] Mean PDI values, SD was ≤0.01.

2.2. Physico-Chemical Characterization of SPIONs

The physico-chemical characterization of SPIONs (**Table 1**) was based on dynamic light scattering, electrophoretic light scattering (ζ-potential determination), and transmission electron microscopy.

Nanoparticles used in the present study had a hydrodynamic diameter below 100 nm and a monodisperse size distribution (PDI ≈ 0.2). All particles were anionic with a ζ-potential of at least –18 mV. Due to a high colloidal stability, they could be stored for prolonged periods of time (>1 month at 4 °C). Fluorescent labeling of the particles had a minor impact on their basic physicochemical characteristics.

The size, morphology and colloidal stability of stabilized SPIONs was visualized by transmission electron microscopy (**Figure 1**). Uncoated SPIONs could not be analyzed due to flocculation and erosion. Agglomeration and degradation of these lipophilic and dense SPION cores can be minimized by appropriate particle coating, see Figure 1—the protein HSA (Figure 1A), the polysaccharide dextran (Figure 1B), phospholipids (Figure 1C), or a combination of phospholipids and PEG of molecular weight 5000 (Figure 1D).

2.3. Cellular Uptake and Cytotoxicity

Interactions of nanoparticles with cells of the immune system can drastically reduce their half-life in the circulation. Tissue resident macrophages will bind and internalize such nanoparticles leading to their accumulation in the liver and the spleen. These cellular interactions can be minimized by steric stabilization of the particles, that is, coating of their surface with hydrophilic polymers such as polyethylene glycol (PEG). In the present study, such interactions with cells of the immune system were studied in cell culture using the human monocytic cell line THP-1. Fluorescent labeled Lipid- and Lipid-PEG-SPIONs were incubated with THP-1 cells differentiated into immature dendritic cells. They were subsequently analyzed by confocal laser scanning

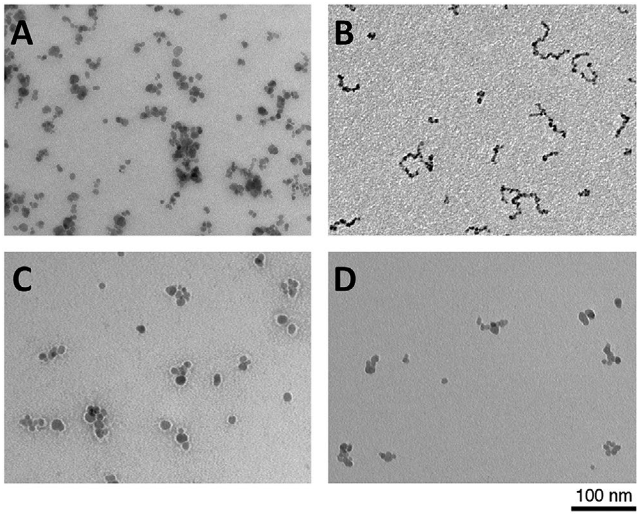

Figure 1. Transmission electron microscope images of SPIONs. Nanoparticles coated with A) human serum albumin (HSA-SPIONs), B) dextran (Dex-SPIONs), and embedded with C) phospholipids without PEG (Lipid-SPIONs), and D) phospholipids containing PEG of MW 5000 (Lipid-PEG-SPIONs). Particle characteristics are summarized in Table 1. Scale bars correspond to 100 nm.

microscopy (**Figure 2**A,B) and flow cytometry (Figure 2C). The phagocytic THP-1 cells rapidly internalize Lipid-SPIONs whereas sterically stabilized Lipid-PEG-SPIONs are not taken up due to the shielding effect of PEG. Qualitative fluorescent microcopy results were confirmed by quantitative flow cytometry analysis (Figure 2C). It should be emphasized, that this type of in vitro experiments can be performed only with fluorescent labeled particles. To exclude any cytotoxic effects of Lipid-SPIONs and Lipid-PEG-SPIONs, MTT, and Alamar blue viability assays were performed. Both lipid coated SPIONs had no negative impact on the viability of THP-1 cells (data not shown).

2.4. Light Microscopy-Based Visualization of SPIONs in the Zebrafish Embryo

In view of limitations imposed by cell culture-based test systems such as the THP-1 model, in vivo experiments were initiated using zebrafish embryos as a vertebrate screening model. Minute amounts of SPIONs (3 nL of a 4.8 mg mL^{-1} solution corresponding to a dose of less than 15 ng) were intravenously injected. Circulation and biodistribution of fluorescent nanoparticles in the zebrafish embryo 72 h post fertilization (hpf) was visualized by confocal microscopy (**Figure 3**A). Again, lipid-SPIONs and Lipid-PEG-SPIONs had to be labeled using the fluorescent, lipophilic, and cationic indocarbocyanine dye DiI (Figure 3B, red signal). To allow for a co-localization of nanoparticles, a transgenic zebrafish line (mpeg:kaede) expressing a green fluorescent protein within macrophages was used (Figure 3B, green signal). Macrophage uptake in vivo was detectable 24 h post injection in the caudal vein region of the embryo. A short half-life in the circulation and rapid sequestration of lipid-SPIONs by macrophages was observed. In contrast, pegylated nanoparticles (Lipid-PEG-SPIONs) had a long half-life in the circulation and apparently evaded macrophage uptake.

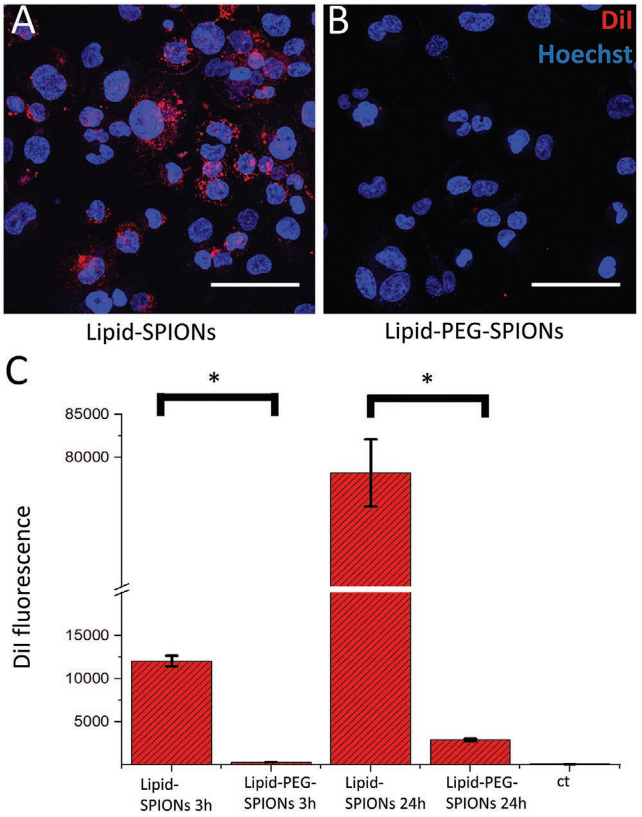

Figure 2. Cellular uptake of fluorescent labeled SPIONs by phagocytic THP-1 cells. Uptake of A) lipid-SPIONs or B) lipid-PEG-SPIONs by phagocytic THP-1 cells. Incubation for 3 h followed by confocal microscopy reveals intracellular location of SPIONs (red signal: DiI labeled SPIONs, blue signal: Hoechst 33342 staining of cell nuclei). Scale bars correspond to 60 µm. C) Quantitative analysis of cellular uptake of DiI labeled SPIONs by flow cytometry analysis after 3 and 24 h incubations. ct: untreated control cells. Values are means ± S.D., $n = 3$. *: Student's t-test, $p < 0.05$.

HSA-SPIONs and Dex-SPIONs used in the present study did not carry a fluorescent label. Therefore, particles had to be co-injected with Prussian blue to allow for an analysis by bright-field microscopy. This dye changes its color from brown to blue in presence of free iron, thus serving as an indicator to discriminate between SPIONs with an intact coating (Figure 3B, brown signal) or agglomerates of partially degraded particles (Figure 3B, blue signal). HSA-SPIONs did accumulate in a tissue compartment below the cardinal vein. A granular blue staining pattern was indicative of agglomeration and degradation. Dex-SPIONs could not be detected suggesting a good coating stability in vivo. To ensure that injected HSA-SPIONs did not cause toxic effects despite their degradation and the associated release of free iron, zebrafish embryo viability and malformation occurrence were monitored for up to 96 h post injection (Table S1, Supporting Information) to confirm absence of toxicity.

2.5. Hard X-Ray Tomography of SPION Biodistribution in Zebrafish Embryos

Exploratory experiments with two laboratory µCT instruments nanotom m (phoenix|x-ray, GE Sensing & Inspection Technologies

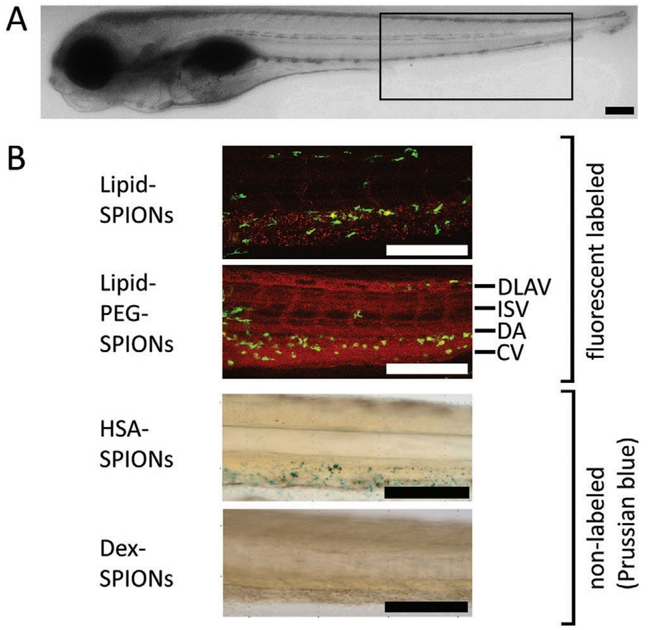

Figure 3. Microscopy based analysis of SPIONs injected into zebrafish embryos. A) Phase-contrast image of a 72 hpf zebrafish embryo. B) Tail section used for visual inspection of particle distribution is highlighted. (top) Confocal microscopy analysis of 72 hpf zebrafish embryos injected with DiI labeled, phospholipid embedded SPIONs (red signal). Macrophages expressing mpeg:kaede are visible in green. (bottom) bright-field images of 72 hpf zebrafish embryos injected with HSA-SPIONs or Dex-SPIONs co-injected with Prussian blue. Embryos were analyzed 24 h post injection. DA: dorsal aorta, CV: cardinal vein, ISV: intersegmental vessel, DLAV: dorsal longitudinal anastomotic vessel. Scale bars correspond to 100 µm.

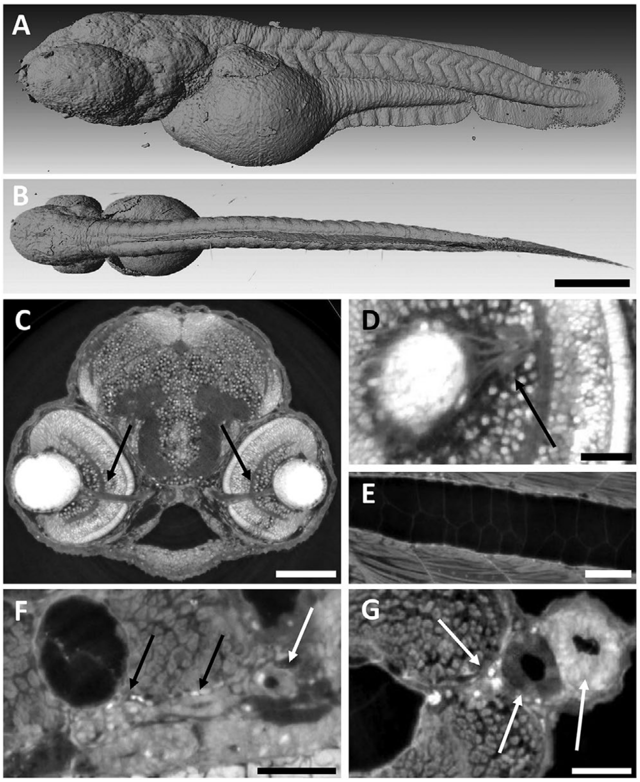

Figure 4. 3D surface rendering and virtual histology of the zebrafish embryo from SRµCT. 3D surface rendering in A) lateral direction and B) dorsal-ventral direction of a 48 hpf zebrafish embryo. C) Virtual tissue sections showing the brain and the eyes of the embryo (transverse plane through the head). The optic nerves are labeled with black arrows. D) Magnification of the eye showing the retina and optical nerve fenestrations (transverse plane, black arrow). E) Notochord with surrounding muscle fibers (midsagittal plane through the tail). F) Pronephron with glomerulus (sagittal plane, dorsal location next to the yolk sac, white arrow) and tubules (black arrows). G) Gut (transverse plane through the tail cranial to the cloaca, right arrow), kidney tubule (middle arrow), and the caudal vein (left arrow). Scale bars correspond to 200 µm (A,B); 70 µm (C,E); 20 µm (D,F,G). Additional high-resolution images are provided on a dedicated internet page (http://zebrafish.pharma-te.ch).

GmbH, Wunstorf, Germany) and Skyscan 1275 (Bruker, Kontich, Belgium) revealed several anatomical features in zebrafish embryos (Figure S1, Supporting Information). The nanotom m measurement showed the outer shape of the embryos (Figure S1A, Supporting Information) and the position of the otoliths (Figure S1B, Supporting Information), but other anatomical features could not be identified because of the detector's energy selectivity, that is, photons below 30 keV are suppressed by the aluminum film in front of the detector. The otoliths have a length of 15–30 µm and consist of crystalline calcium carbonate, that is, aragonite with a density of 2.83 g cm^{-3}[26] and are very well resolved in µCT.[27] The Skyscan 1275 system allows detecting photons with energies as low as 10 keV. Therefore, many additional details including eye, eye lens, spine and yolk were identified with a spatial resolution of about 8 µm.

In order to increase the spatial and density resolution with respect to advanced laboratory-based µCT, SRµCT was explored. Combined absorption- and phase-contrast revealed a wealth of anatomical structures of dehydrated and ethanol-fixed zebrafish embryos 48 hpf. An effective voxel size of 330 nm was selected and three vertically stacked tomograms were acquired to completely visualize the zebrafish embryo with a size of $3.0 \times 1.0 \times 0.5$ mm^3, resulting in 1.4×10^7 voxels. The spatial resolution was around 2 µm, as measured in the reconstructed slices.[28,29]

3D surface renderings reveal honeycomb-like structures on the yolk and eye surface, muscles were in the tail region behind the yolk of the zebrafish embryo, and fins laterally at the yolk (**Figure** 4A,B). Virtual slices at arbitrary position and angle through the 3D volume allow for inspection of the anatomy on the micrometer scale. For example, the structure of the eye including the retina and the visual nerve, the brain, the gastrointestinal (GI) tract and the kidneys are revealed with high detail (Figure 4C–G).

Additional stacks of 100 slices in cranial-caudal, ventral-dorsal, and lateral directions are provided for one 48 hpf zebrafish embryo on a dedicated internet site (http://zebrafish.pharma-te.ch). In the head region of these projections, the four otoliths of each zebrafish are clearly visible due to their high density and X-ray attenuation. They may serve as reference points of an imaginary coordinate system.

To visualize tissue distribution of SPIONs, SRµCT imaging was performed 24 h post injection of coated SPIONs (**Figure 5**). To exploit phase contrast, single-distance phase retrieval was performed prior to tomographic reconstruction.[30] Maximum intensity projections of the resulting 3D datasets allow for

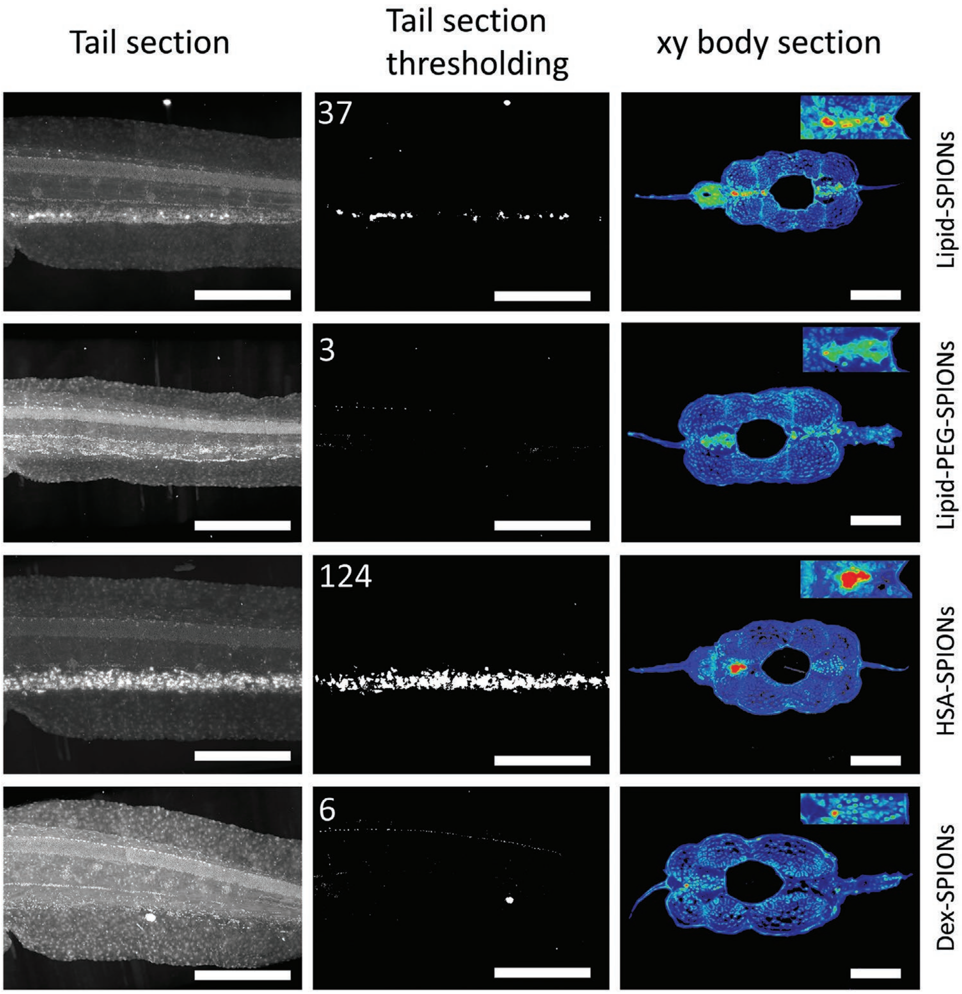

Figure 5. Localization of SPIONs by SRμCT in the tail section of 72 hpf zebrafish embryos. Maximum intensity projections of the tail section behind the cloaca of the zebrafish embryos 24 h post injection of SPIONs. Left column: maximum intensity projections onto the lateral plane. Center column: visualization of SPION agglomerates based on threshold value segmentation of intensity projections shown in the left column. Numbers refer to the number of identified particle agglomerates. Right column: tail sections through the cranial-caudal (*x*–*y*) plane. Visualization by false coloring of high-density agglomerates representing SPIONs. Color gradient from blue (low density) to red (high density). Insert: magnification of the caudal vein. Left and central column scale bars correspond to 300 μm; right column scale bars correspond to 50 μm.

differentiating SPIONs, eye lenses, otoliths, and soft tissue. The injected SPIONs could be localized based on just the higher density of their iron core, confirming that precise localization of non-labeled SPIONs is possible. A single threshold was applied to all four maximum intensity projections to segment the SPION agglomerates. SPIONs were distributed throughout the vascular system and accumulated in the vicinity of the caudal vein as well as the dorsal artery (Figure 5). Particles coated with PEG of MW 5000 (Lipid-PEG-SPIONs) or dextran (Dex-SPIONs) showed no agglomeration whereas particles without steric stabilization (Lipid-SPIONs) or HSA-SPIONs showed extensive agglomeration and deposition within the caudal vein in the tail region. A high-contrast colormap applied to the transverse plane through the tail further confirms these findings. It should be noted, that SPION derived high-density signals can be combined with high-resolution SRμCT tissue representations, see **Figure 6**, which provides a comparable spatial resolution and, but enhanced anatomical details, as compared to light or confocal microscopy, see Figure 3. The nanoparticles are well separated from other strongly X-ray-absorbing features such as the otoliths. Therefore, the authors selected the region

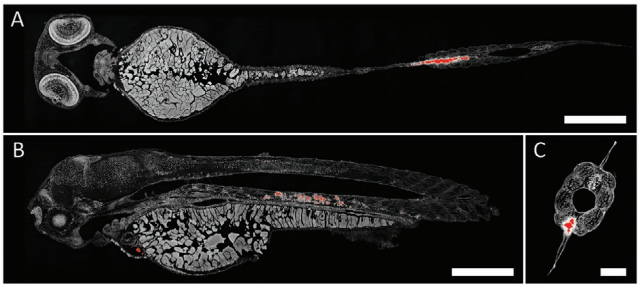

Figure 6. Localization of SPIONs by SRμCT. High resolution SRμCT sections of zebrafish embryos 24 h post injection of SPIONs (density-based red signal). A) coronal plane, B) sagittal plane, and C) transverse plane. Scale bars correspond to 200 μm (A and B), 50 μm (C).

of interest with the nanoparticles and an appropriate threshold to determine the total volume of the aggregated nanoparticles, which corresponds to 220 pL. The nanoparticles volume injected amounts to 2.8 pL. There is a considerable ratio between the nanoparticles volume identified and the one injected, namely about 80. The reasons behind are i) partial volume phenomena and ii) the smear-out by the application of the Paganin algorithm. Furthermore, the authors are convinced that the nanoparticles form loosely packed agglomerates making them to an efficient contrast agent in X-ray imaging.

3. Discussion

SPIONs used in the present study were characterized according to established principles.[10,31,32] They had a similar size, a negative ζ-potential, a high colloidal stability, and a monodisperse size distribution. SPIONs were not cytotoxic and well tolerated in vivo. Neither the MTT assay nor the Alamar blue assay showed statistically significant differences with respect to THP-1 viability as compared to untreated controls confirming previous results with HSA-SPIONs[23] and Dex-SPIONs.[24] Maximal concentrations in these assays were 96 µg mL^{-1} (96 ppm) to avoid catalytic or optical interference of tested particles. It is reasonable to assume that particle concentrations reached in blood in vivo are comparable to these concentrations. The total blood volume of the zebrafish is ≈80 nL. The injected volumes with a particle concentrations 4.8 mg mL^{-1} were 3 nL. Thus, the ratio 14.4 ng/80 nL corresponds to about 180 ppm. Upon injection the particles rapidly started to extravasate and distribute within the organism. Since the volume of the fish is substantially larger than the blood volume, we can reasonably expect nanoparticle concentrations within the studied nanotoxicological range.

Bright-field and fluorescence microscopy[33–35] were used to analyze SPIONs. Both light microscopy methods confirm findings from the SRµCT experiments in that HSA-SPIONs and non-pegylated SPIONs (in contrast to pegylated SPIONs or Dex-SPIONs) had a short half-life in the circulation and did accumulate in the caudal vein. The light microscopy methods used confirm the findings from the SRµCT experiments. Contrary to the pegylated SPIONs or Dex-SPIONs, the HSA-SPIONs and non-pegylated SPIONs had a short half-life in circulation and did accumulate mainly in the caudal vein and heart 24 h *post injection*. Prussian blue co-injection provided information on particle integrity since reaction of Prussian blue with iron ions leads to the formation of a blue colored complex.[36] However, samples could be visualized in 2D only by bright field microscopy. Confocal laser scanning microscopy allows for 3D scanning of samples and offers a better sensitivity. Furthermore, different fluorescent labels can be combined to co-localize particles with cellular or anatomical structures. In particular, co-localization of non-pegylated SPIONs with macrophages provides information on the cellular fate of these particles. Live imaging of fish embryos is possible. Still, the requirement of labeling SPIONs for this method is a drawback. We therefore decided to combine these methods with X-ray micro-computed tomography (µCT).

Preliminary experiments based on a laboratory µCT instrument were ultimately unable to reveal the zebrafish embryo micro-anatomy and SPION distribution (Figure S1, Supporting Information). Although spatial resolution was approximately equal to that of the SRµCT (2 µm), density resolution was not satisfactory for the simultaneous visualization of soft tissues and SPIONs. The improved density resolution of SRµCT can be attributed to three factors. First, significantly higher X-ray flux, with 200 000 counts s^{-1} for the SRµCT compared to 260 counts s^{-1} for µCT, allowed for both a faster acquisition time and improved photon statistics. Second, the lower photon energy for SRµCT, which was 10.25 keV compared to the 40 kV acceleration voltage (≈30 keV mean energy) of the laboratory µCT meant that the photon efficiency was greater for the SRµCT.[37] This is not an inherent limitation of laboratory µCT, rather the particular instrument employed in this study has a medical X-ray detector with an aluminum coating that absorbs lower energy photons. Third, the high temporal and spatial coherence of the X-ray beam provided by the synchrotron source allow for access to the phase information. Single-distance phase retrieval was applied and provided improved contrast-to-noise ratio, though at the expense of some spatial resolution. It should be noted that a major advantage of laboratory sources is the accessibility. Furthermore, developments in advanced laboratory systems allow for excellent flux and sufficient coherence for high quality phase contrast imaging of biological specimens. This will offer interesting possibilities in the near future.[38,39]

In view of the limitations imposed by laboratory µCT, we decided to use SRµCT as an alternative method to localize non-labeled SPIONs within the vasculature of the zebrafish embryo based on the inherent electron density differences between the nanoparticles and biological tissues. Indeed, it was possible to visualize SPIONs and anatomical structures at a cellular resolution with unprecedented detail. With respect to the established murine and rat models,[40–42] the zebrafish embryos are an attractive alternative for pharmacokinetics and pharmacology studies of nanoparticles due to their small size, the possibility to perform screening experiments in a vertebrate, reduced costs, and ethical aspects. Pegylated SPIONs (Lipid-PEG-SPIONs) and Dex-SPIONs did not form agglomerates or tissue deposits, indicating a long half-life in the circulation. These results were in line with uptake experiments in phagocytic THP-1 cells, where pegylated SPIONs showed minimal cellular uptake. In contrast, agglomerates of particles without steric stabilization or HSA-SPIONs were deposited in the caudal vein or the tail region of the zebrafish embryo suggesting a rapid uptake by tissue resident macrophages.[43] It should be noted that the high X-ray intensity led to formation of gas bubbles and motion artefacts in the medium surrounding the specimen if aqueous buffers were used. We therefore had to replace the medium by ethanol. Consequently, imaging of living specimens was impossible, at least for the spatial and density resolution achieved in this study. No structural change of the fixed zebrafish embryo was observed over the course of the tomographic acquisition. The radiation dose of ≈160 kGy, however, is too high for in vivo studies. In comparison with alternative methods including MR microscopy, SRµCT provides at least one order of magnitude better spatial resolution in each of the three orthogonal directions.[44] Thus, the information gain in tomographic imaging is at least 1000.

The contrast mechanism in SRµCT differs from optical microscopy. In the photon energy range used, the photo effect yields X-ray attenuation, which linearly depends on the density and from the atomic number by a power law. The SPION exhibits strong X-ray absorption and, thus become visible at low concentrations. The main advantage of SRµCT with respect to conventional and advanced optical methods is the isotropic spatial resolution in the three orthogonal directions. Therefore, 3D pharmacokinetics and pharmacology studies based on absorption, distribution, metabolism, and excretion (ADME) should become more reliable especially for larger organisms.

Because the contrast mechanisms of the optical and X-ray-based techniques have dedicated origin, a combination of the methods can be beneficial, although the lateral spatial resolution is almost equal.[44] A bivariant histogram of data from a selected individuum may lead to information inaccessible by a single method.[45]

The wavelength of hard X-ray tomography is below one nanometer, which implies that the diffraction limit is three orders of magnitude smaller than for optical methods. Therefore, the use of X-ray optics has pushed the spatial resolution of synchrotron radiation-based computed tomography to values well below 100 nm.[46]

It should be mentioned that SRµCT has further advantages with respect to laboratory-based systems. First, the photon energy can be selected in an optimized fashion, for example by applying the Grodzins' criterion.[37] Second, one can acquire data above and below an absorption edge to derive the 3D distribution of the selected element. Concentrations as low as 10 ppm have been detected for osmium.[47] In order to determine the iron distribution within the zebrafish embryo, tomography data just above and below the K-edge (7.1 keV) have to be recorded. At the TOMCAT beamline photon energies below 8 keV are inaccessible. Other imaging beamlines such as P05 at PETRA III, Hamburg, Germany[48] are suited for such a task. Hence, one can reasonably expect future high-resolution tomography studies using synchrotron radiation.

4. Conclusion

Label-free, non-destructive monitoring of low-dose metal-based nanoparticles in an entire vertebrate embryo at submicron voxel sizes was achieved using SRµCT. Analysis based on single-distance phase-contrast provides insight into micro-anatomical structures of zebrafish embryos at a defined developmental stage. For example, structures such as the retina, the optical nerve or the renal tubular system could be examined in their natural state without staining and slicing the specimen. It is tempting to speculate that application of SRµCT for medical diagnostics might offer similar insights. In such a scenario, fast visualization of anatomical structures within small samples of native soft tissue such as, for example, needle biopsies could become a clinical routine.

5. Experimental Section

Synthesis of Superparamagnetic Iron Oxide Nanoparticles Coated with Human Serum Albumin (HSA-SPIONs): Superparamagnetic iron oxide nanoparticles (SPIONs) coated with human serum albumin ($SEON^{LA17HSA2}$) and dextran ($SEON^{Dex-36q}$) were synthesized as described previously.[23,24] In the present publication, they were designated as HSA-SPIONs and Dex-SPIONs.

Synthesis of Iron Oxide Nanoparticles (SPIONs): SPIONs were synthesized as described previously.[22] In brief, iron(II) chloride ($FeCl_2$) and iron(III) chloride ($FeCl_3$) aqueous solutions (0.024 M $FeCl_2$, 0.037 M $FeCl_3$ in 20 mL milliQ water) were combined at a molar ratio of 3:2 and filtered through a 0.22 µm polycarbonate membrane to remove undissolved agglomerates. By adding concentrated ammonia (30% aqueous solution) at room temperature, co-precipitation took place with an immediate black precipitate formation. The precipitate was washed three times with diluted ammonia (1.5% aqueous solution). Oleic acid (1 g) was added and the solution was heated for 5–10 min to 90 °C. With the help of a magnet, the particles were transferred to trichloromethane. These lipophilic particles were stable for at least 6 months at 4 °C.

Microfluidics Based Preparation of Lipid Coated SPIONs: Lipid-SPIONs and Lipid-PEG-SPIONs, respectively, were prepared using a microfluidics benchtop instrument (NanoAssemblr, Precision Nanosystems, Vancouver, Canada). SPIONs (5 mg) in trichloromethane were dried by evaporation of the solvent and dissolved again in the same volume of a mixture of 60:40 (v/v) of ethanol:tetrahydrofurane containing 1.3 µM cholesterol and 1.63 µM POPC (Avanti Polar Lipids, Alabaster, AL, USA). Where indicated, part of POPC was replaced by an equal molar amount of indocarbocyanine fluorescent dye (0.03 µM) and/or DSPE modified with PEG of molecular weight 5000 (0.33 µM) (Avanti Polar Lipids). As the admixed hydrophilic phase, phosphate buffered saline (10 mM phosphate, 150 mM NaCl, pH of 7.4) was used. The flow rate ratio organic phase:aqueous phase was 2:1 and the flow rate was 10 mL min^{-1}. Liposome-coated SPIONs were dialyzed against PBS overnight using a Spectra/Por2 dialysis membrane with a MW cut-off of 12–14 kDa (Spectrum Europe BV., DG Breda, The Netherlands) to remove organic solvents. After dialysis, samples were purified by size exclusion chromatography (NAP-10 Sephadex G25 column (Sigma Aldrich, St. Louis, MO, USA) to remove uncoated iron oxide nanoparticles/free iron from the solution. Concentrations of SPIONs were determined based on their optical density (OD) in trichloromethane at 520 nm using stock solutions of uncoated SPIONS in trichloromethane (see above) as a reference.

Physico-Chemical Characterization of Nanoparticles: Analysis of particle size, hydrodynamic diameter, polydispersity index, and ζ potential of lipid-(PEG-)SPIONs were performed as described.[49] The used methods were dynamic and electrophoretic light scattering (Delsa Nano C, Beckman Coulter Inc., Nyon, Switzerland) and transmission electron microscopy (CM-100, Philips, Amsterdam, Netherlands).

Cellular Uptake of SPIONs by THP-1 Phagocytic Cells: THP-1 monocytic cells (acute monocytic leukemia, human, ATCC, TIB-202) were cultured in Roswell Park Memorial Institute 1640 (RPMI 1640) cell medium (supplemented with 10% foetal calf serum, penicillin (100 units mL^{-1})/streptomycin (100 µg mL^{-1}), 10 mM HEPES buffer, 1% sodium pyruvate, and 0.05 mM ß-mercaptoethanol). The cell medium was renewed every 3 days. For uptake studies, THP-1 cells were seeded at a density of 5×10^4 cells per well onto poly-d-lysine-coated 8-Well µ-Slides (Ibidi, Martinsried, Germany). Differentiation to macrophages was induced by addition of 200 nM phorbol 12-myristate 13-acetate (PMA) for 72 h. For uptake studies, cells were incubated with fluorescent labeled SPIONs (48 µg mL^{-1} iron oxide concentration) in cell culture medium. Cells were washed with PBS buffer, cell nuclei were counterstained using Hoechst 33342 (2.5 µg mL^{-1}) for 10 min and cell membranes were counterstained using CellMask Deep Red Plasma membrane stain (0.5 µL mL^{-1}) for 5 min (both Thermo Fisher Scientific Inc., Waltham, MA, USA). Cells were washed with cell culture medium and analyzed by confocal laser scanning microscopy (see below).

Quantitative analysis of cellular uptake was performed by flow cytometry (FACS) using a BD FACSCanto II RUO Special Order System (BD Biosciences, Allschwil, BL, Switzerland). Cells were incubated with fluorescent labeled lipid-(PEG-)SPIONs as described above, washed with PBS, and collected by trypsinization (5 min at 37 °C). After centrifugation in Eppendorf tubes, the pellets were resuspended in PBS and measured in the flow cytometer (10 000 counts, FL-6 laser).

Cytotoxicity: To determine cell viability, MTT,[50] and Alamar blue[51] assays were used in combination with THP-1 and Hep G2 cells.[50] For the Alamar blue assay, fluorescence was measured with an excitation at 560 nm and an emission at 580 nm (Spectramax M2 plate reader, Molecular Devices, Sunnyvale, CA) 4 h after addition of a 10% of Alamar blue solution. Cytotoxicity was expressed as the percentage of viable cells, where untreated cells were defined to be 100% viable. Each time point had its own 100% viability control. Since high concentrations of SPIONs were known to interfere with the MTT or Alamar blue assays, control experiments were carried out to exclude catalytic or optical interference of SPIONs (up to 96 µg mL^{-1}) in incubations of up to 48 h.

Zebrafish Barge Culture: Experiments were conducted using zebrafish embryos (Danio rerio) from the wildtype strain AB/Tübingen (AB/Tu) and transgenic strain mpeg:kaede (Tg(mpeg1:Gal4-VP16/UAS:Kaede)) with fluorescent macrophages.[52] Adult zebrafish were kept in 20 L aerated tanks at a temperature of 28 °C and a 10/14 h light/dark cycle. Mating was carried out in breeding baskets. Eggs were collected the next morning, cleaned, sorted, and transferred into petri dishes containing 25 mL of embryo-medium E2 as described previously.[43] A maximum of 100 eggs were transferred into one petri dish and stored in an incubator (Aqualytic, Dortmund, Germany) at 28 °C. E2 medium was renewed daily after egg sorting. 24 h post fertilization (hpf) the embryos were bleached with 200 µM 1-phenyl 2-thiourea (PTU) to inhibit melanization. Zebrafish embryos were dechorionated 48 hpf.

Bright-Field or Phase-Contrast Microscopy: The zebrafish embryos were fixed in 4% PFA for 30 min and dehydrated with increasing ethanol dilutions series from 25, 50, 75, and >96 vol% for 15 min each and stored in analytical ethanol (>96 vol%). Each embryo was embedded using Euparal embedding medium (Carl Roth, Karlsruhe, Germany) on microscope slides and dried for 3 days. For analyzing and imaging, a Leica DM6000 microscope (Leica Microsystems, Heerbrugg, Switzerland) was used.

Confocal Laser Scanning Microscopy: 48 hpf zebrafish embryos were sedated, immobilized and injected with lipoSPIONs as described below and were placed on glass bottom petri dishes for imaging. Confocal scanning microscopy was done with a ZEISS LSM 880 inverted microscope (Carl Zeiss, Oberkochen, Germany). Z-stacks were recorded at a step size of 100 µm using a 40 × objective (N.A. 1.1). Excitation wavelength was 488 nm (mpeg:kaede), and 561 nm (DiI) in combination with bright-field microscopy. The emission wavelength covered ranges from 500 to 535 nm and 575 to 636 nm, respectively. Image stacks were processed using the open source Fiji software (ImageJ, Version 1.52p, Wayne Rasband, Research Services Branch, National Institute of Mental Health, Bethesda, Maryland, USA).[53]

Zebrafish Injection and Fixation: For the experiments, the embryos were anaesthetized with 25 mL of tricaine methanesulfonate (612 µM) in E2 fish media. They were immobilized in 0.3% agarose containing tricaine methanesulfonate (612 µM) and placed on glass bottom petri dishes (MatTek, Ashland, MA, USA), each laying on the left side. Microinjections of NP were conducted as described previously.[43] Injected nanoparticle volumes were 3 nL for all types of SPIONs (4.8 mg mL^{-1}).

For micro-tomography experiments, embryos (1 and 24 h post injection (hpi) of SPIONs) were euthanized with tricaine methanesulfonate containing 0.612 mM trisaminomethane. Subsequently, embryos were fixed at room temperature for 1 hin 4.0% paraformaldehyde. Fixed specimens were dehydrated using ethanol at increasing concentrations (25%, 50%, 70%, and ≥99.8%) for 15 min each under gentle agitation and stored at 4 °C.

Sample Preparation for X-Ray Tomography: Embryos fixed in ethanol were placed within sample holders consisting of plastic pipette tips filled with ethanol. Using ethanol as a solvent (in contrast to an aqueous buffer or UV sensitive polymers[54]) avoided formation of gas bubbles during X-ray irradiation.

SRµCT: Single-distance phase-contrast SRµCT was used for 3D visualization of nanoparticles injected into zebrafish embryos. Experiments were performed at the Swiss Light Source (Villigen, Switzerland) TOMCAT X02DA beamline. Here, a superbending magnet source combined with a Si(111) double crystal monochromator produced a monochromatic beam with a photon energy of 10.25 keV ($\Delta E/E \approx 10^{-4}$). For single-distance phase retrieval, the sample-detector distance was 12 mm. The source size was ≈140 µm × 45 µm (h × v), corresponding to a projected source size of 64 nm × 21 nm. Thus, the spatial resolution was limited by other factors such as detector pixel size and scintillator thickness. This setup provides significantly higher transverse and longitudinal coherence compared to laboratory X-ray sources. Projections were recorded using a LuAG:Ce scintillator coupled to a pco.EDGE 5.5 camera (2560 × 2160 pixel array and 16 bit depth) with the UPLAPO10x (effective pixel size 0.65 µm) and UPLAPO20x (effective pixel size 0.325 µm) objectives. In order to visualize the entire specimen, three to five height steps per specimen were acquired depending on the post fertilization stage. An exposure time of 240 ms was selected (around 50 000 counts per flat field) for 1801 projections recorded around 180° resulting in total scan times of around 7 min.

Reconstruction of Micro-Tomograms: Phase retrieval for the SRµCT projections was performed with the single distance non-iterative method introduced by Paganin and co-workers[30] as implemented in AnkaPhase (Version 2.1).[55] Reconstruction was performed in TomoPy with ASTRA Toolbox 1.8, an open-source Python package for tomographic data processing and image reconstruction.[56,57] A δ/β value of 10^3 was used to obtain optimized contrast and to reduce edge enhancement for the monitoring of the SPIONs. It should be noted that data were acquired far from the criterion presented by Grodzins for optimized absorption contrast, which was a well-known rule-of-thumb although it was only strictly valid for single phase materials and the central point. Additionally, with photon energy of 10.25 keV and pixel size of 325 nm, the propagation distance of 12 mm was outside of the contact plane for a pure absorption measurement.

Analysis of the Reconstructed Data: Spatial resolution was estimated on reconstructed slices with the method proposed by Mizutani and co-workers as well as the method proposed by Modregger and co-workers.[28,29] 3D surface renderings and maximum intensity projections were generated using the 3D visualization and analysis software Avizo (Version 9.5, FEI Visualization Sciences Group, Hillsboro, OR, USA). Specific regions of interest (e.g. whole zebrafish embryo, otoliths, nanoparticle agglomerates) were segmented by thresholding. Virtual histological sections were created by analyzing the ortho slices in each direction of the 3D volume. Free access to this data set in the form of collections of high resolution images is provided on a dedicated internet page (http://zebrafish.pharma-te.ch).

Statistical Analysis: Results were expressed as means of independent sets of experiments ± standard deviation (SD), $n \geq 3$. Wherever indicated, significance was determined by one-way analysis of variance (ANOVA). Tukey's post-hoc test was performed to compare the difference between treated groups and corresponding controls. Differences were considered to be significant at $p \leq 0.05$. Used software was Origin 9.1 (OriginLab, Northampton, MA, USA).

Supporting Information

Supporting Information is available from the Wiley Online Library or from the author.

Acknowledgements

This work was supported by grants from the Swiss Center for Applied Human Toxicology (SCAHT), the NanoReg2 program (European Union Horizon 2020 research agreement 646221, 15.0200-3), the Manfred Roth Foundation, Fürth, Germany and the Forschungsstiftung Medizin, University Hospital Erlangen, Germany. The authors thank Prof. Markus Affolter, Dr. Heinz Belting, and Dr. Susanne Schenk for support with zebrafish barge culturing. The authors acknowledge the Paul Scherrer

Institut, Villigen, Switzerland for provision of synchrotron radiation beamtime at the TOMCAT beamline X02DA of the SLS.

Conflict of Interest

The authors declare no conflict of interest.

Keywords

digital histology, nanoparticle detection, superparamagnetic iron oxide nanoparticles, synchrotron radiation-based micro computed tomography, zebrafish embryos

Received: March 11, 2020
Revised: May 26, 2020
Published online:

---

[1] R. Tietze, H. Rahn, S. Lyer, E. Schreiber, J. Mann, S. Odenbach, C. Alexiou, *Histochem. Cell Biol.* **2011**, *135*, 153.
[2] A. Wicki, D. Witzigmann, V. Balasubramanian, J. Huwyler, *J. Controlled Release* **2015**, *200*, 138.
[3] D. D. Jurašin, M. Ćurlin, I. Capjak, T. Crnković, M. Lovrić, M. Babič, D. Horák, I. V. Vrček, S. Gajović, *Beilstein J. Nanotechnol.* **2016**, *7*, 246.
[4] M. Bietenbeck, A. Florian, C. Faber, U. Sechtem, A. Yilmaz, *Int J Nanomed.* **2016**, *11*, 3191.
[5] R. Tietze, J. Zaloga, H. Unterweger, S. Lyer, R. P. Friedrich, C. Janko, M. Pöttler, S. Dürr, C. Alexiou, *Biochem. Biophys. Res. Commun.* **2015**, *468*, 463.
[6] L. Yildirimer, N. T. K. Thanh, M. Loizidou, A. M. Seifalian, *Nano Today* **2011**, *6*, 585.
[7] M. E. Samberg, S. J. Oldenburg, N. A. Monteiro-Riviere, *Environ. Health Perspect.* **2010**, *118*, 407.
[8] Y.-S. Chen, Y.-C. Hung, I. Liau, G. S. Huang, *Nanoscale Res. Lett.* **2009**, *4*, 858.
[9] C. C. Hanot, Y. S. Choi, T. B. Anani, D. Soundarrajan, A. E. David, *Int. J. Mol. Sci.* **2016**, *17*, 54.
[10] S. Siegrist, E. Cörek, P. Detampel, J. Sandström, P. Wick, J. Huwyler, *Nanotoxicology* **2018**, *13*, 73.
[11] G. D. Rubin, *Radiology* **2014**, *273*, S45.
[12] M. Shilo, T. Reuveni, M. Motiei, R. Popovtzer, *Nanomedicine.* **2012**, *7*, 257.
[13] J. R. Ashton, J. L. West, C. T. Badea, *Front. Pharmacol.* **2015**, *6*, 256.
[14] D. P. Clark, C. T. Badea, *Phys. Med.* **2014**, *30*, 619.
[15] D. P. Cormode, P. C. Naha, Z. A. Fayad, *Contrast Media Mol. Imaging* **2014**, *9*, 37.
[16] R. Meir, R. Popovtzer, *Wiley Interdiscip. Rev. Nanomed. Nanobiotechnol.* **2018**, *10*, 28544497.
[17] L. Y. Rizzo, S. K. Golombek, M. E. Mertens, Y. Pan, D. Laaf, J. Broda, J. Jayapaul, D. Möckel, V. Subr, W. E. Hennink, G. Storm, U. Simon, W. Jahnen-Dechent, F. Kiessling, T. Lammers, *J. Mater. Chem. B* **2013**, *1*, 3918.
[18] C. Chakraborty, A. R. Sharma, G. Sharma, S.-S. Lee, *J. Nanobiotechnol.* **2016**, *14*, 65.
[19] B. Novoa, A. Figueras, in *Curr. Top. Innate Immun. II* (Eds.: J. D. Lambris, G. Hajishengallis), Springer, New York, NY **2012**, pp. 253–275.
[20] S. Sieber, P. Grossen, J. Bussmann, F. Campbell, A. Kros, D. Witzigmann, J. Huwyler, *Adv. Drug Delivery Rev.* **2019**, *151–152*, 152.
[21] M. Dalstra, P. M. Cattaneo, F. Beckmann, *J. Craniofacial Genet. Dev. Biol.* **2006**, *9*, 199.
[22] M. D. Cuyper, M. Joniau, *Eur. Biophys. J.* **1988**, *15*, 311.
[23] J. Zaloga, M. Pöttler, G. Leitinger, R. P. Friedrich, G. Almer, S. Lyer, E. Baum, R. Tietze, R. Heimke-Brinck, H. Mangge, F. Dörje, G. Lee, C. Alexiou, *Eur. J. Pharm. Biopharm.* **2016**, *101*, 152.
[24] H. Unterweger, C. Janko, M. Schwarz, L. Dézsi, R. Urbanics, J. Matuszak, E. Őrfi, T. Fülöp, T. Bäuerle, J. Szebeni, C. Journé, A. R. Boccaccini, C. Alexiou, S. Lyer, I. Cicha, *Int. J. Nanomed.* **2017**, *12*, 5223.
[25] M. Sedighi, S. Sieber, F. Rahimi, M.-A. Shahbazi, A. H. Rezayan, J. Huwyler, D. Witzigmann, *Drug Delivery Transl. Res.* **2019**, *9*, 404.
[26] C. Haddon, J. Lewis, *J. Comp. Neurol.* **1996**, *365*, 113.
[27] B. Müller, R. Bernhardt, T. Weitkamp, F. Beckmann, R. Bräuer, U. Schurigt, A. Schrott-Fischer, R. Glueckert, M. Ney, T. Beleites, C. Jolly, D. Scharnweber, *Int. J. Mater. Res.* **2007**, *98*, 613.
[28] R. Mizutani, R. Saiga, S. Takekoshi, C. Inomoto, N. Nakamura, M. Itokawa, M. Arai, K. Oshima, A. Takeuchi, K. Uesugi, Y. Terada, Y. Suzuki, *J. Microsc.* **2016**, *261*, 57.
[29] P. Modregger, D. Lübbert, P. Schäfer, R. Köhler, *Phys. Status Solidi A* **2007**, *204*, 2746.
[30] D. Paganin, S. C. Mayo, T. E. Gureyev, P. R. Miller, S. W. Wilkins, *J Microsc.* **2002**, *206*, 33.
[31] S. S. Khiabani, M. Farshbaf, A. Akbarzadeh, S. Davaran, *Artif. Cells, Nanomed., Biotechnol.* **2017**, *45*, 6.
[32] E. J. Cho, H. Holback, K. C. Liu, S. A. Abouelmagd, J. Park, Y. Yeo, *Mol. Pharmaceutics* **2013**, *10*, 2093.
[33] D. E. Igartúa, P. L. Azcona, C. S. Martinez, S. delV. Alonso, V. L. Lassalle, M. J. Prieto, *Toxicol. Appl. Pharmacol.* **2018**, *358*, 23.
[34] M. Giannaccini, M. Giannini, M. P. Calatayud, G. F. Goya, A. Cuschieri, L. Dente, V. Raffa, *Int. J. Mol. Sci.* **2014**, *15*, 1590.
[35] L. C. Felix, V. A. Ortega, J. D. Ede, G. G. Goss, *Environ. Sci. Technol.* **2013**, *47*, 6589.
[36] G. Fu, S. T. Sanjay, X. Li, *Analyst* **2016**, *141*, 3883.
[37] L. Grodzins, *Nucl. Instrum. Methods Phys. Res.* **1983**, *206*, 541.
[38] T. Tuohimaa, M. Otendal, H. M. Hertz, *Appl. Phys. Lett.* **2007**, *91*, 074104.
[39] M. Bartels, V. H. Hernandez, M. Krenkel, T. Moser, T. Salditt, *Appl. Phys. Lett.* **2013**, *103*, 083703.
[40] J. Hu, S. Ni, Y. Cao, X. Wang, S. Liao, H. Lu, *SPINE* **2017**, *42*, E883.
[41] M. Saccomano, J. Albers, G. Tromba, M. D. Radmilović, S. Gajović, F. Alves, C. Dullin, *J. Synchrotron Radiat.* **2018**, *25*, 1153.
[42] Y. C. Liyuan Jiang, Y. C. Liyuan Jiang, *Aging Dis.* **2020**, *11*, 1.
[43] S. Sieber, P. Grossen, P. Uhl, P. Detampel, W. Mier, D. Witzigmann, J. Huwyler, *Nanomedicine* **2019**, *17*, 82.
[44] G. Schulz, C. Waschkies, F. Pfeiffer, I. Zanette, T. Weitkamp, C. David, B. Müller, *Sci. Rep.* **2012**, *2*, 826.
[45] A. K. Stalder, B. Ilgenstein, N. Chicherova, H. Deyhle, F. Beckmann, B. Müller, S. E. Hieber, *Int. J. Mater. Res.* **2014**, *105*, 679.
[46] A. Khimchenko, C. Bikis, A. Pacureanu, S. E. Hieber, P. Thalmann, H. Deyhle, G. Schweighauser, J. Hench, S. Frank, M. Müller-Gerbl, G. Schulz, P. Cloetens, B. Müller, *Adv. Sci.* **2018**, *5*, 1700694.
[47] B. Müller, A. Lareida, F. Beckmann, G. M. Diakov, F. Kral, F. Schwarm, R. Stoffner, A. R. Gunkel, R. Glueckert, A. Schrott-Fischer, J. Fischer, A. Andronache, W. Freysinger, in *Developments in X-Ray Tomography V* (Ed:. U. Bonse), SPIE, Bellingham, WA **2006**, p. 631805.
[48] F. Wilde, M. Ogurreck, I. Greving, J. U. Hammel, F. Beckmann, A. Hipp, L. Lottermoser, I. Khokhriakov, P. Lytaev, T. Dose, H. Burmester, M. Müller, A. Schreyer, *AIP Conf. Proc.* **2016**, *1741*, 030035.
[49] S. Siegrist, H. Kettiger, E. Fasler-Kan, J. Huwyler, *Toxicol. In Vitro* **2017**, *42*, 308.
[50] H. Kettiger, D. Sen Karaman, L. Schiesser, J. M. Rosenholm, J. Huwyler, *Toxicol. In Vitro* **2015**, *30*, 355.
[51] R. Hamid, Y. Rotshteyn, L. Rabadi, R. Parikh, P. Bullock, *Toxicol. In Vitro* **2004**, *18*, 703.
[52] F. Ellett, L. Pase, J. W. Hayman, A. Andrianopoulos, G. J. Lieschke, *Blood* **2011**, *117*, e49.

[53] J. Schindelin, I. Arganda-Carreras, E. Frise, V. Kaynig, M. Longair, T. Pietzsch, S. Preibisch, C. Rueden, S. Saalfeld, B. Schmid, J.-Y. Tinevez, D. J. White, V. Hartenstein, K. Eliceiri, P. Tomancak, A. Cardona, *Nat. Methods* **2012**, *9*, 676.
[54] J. Wang, A. Goyanes, S. Gaisford, A. W. Basit, *Int. J. Pharm.* **2016**, *503*, 207.
[55] T. Weitkamp, D. Haas, D. Wegrzynek, A. Rack, *J. Synchrotron Radiat.* **2013**, *20*, 205.
[56] D. Gürsoy, F. De Carlo, X. Xiao, C. Jacobsen, *J. Synchrotron Radiat.* **2014**, *21*, 1188.
[57] D. M. Pelt, D. Gürsoy, W. J. Palenstijn, J. Sijbers, F. De Carlo, K. J. Batenburg, *J. Synchrotron Radiat.* **2016**, *23*, 842.